An Injection Circuit Coupling Impedance Matching Converter and Its Compromised Control Method of Automobile-Based Electromagnetic Prospecting Transmitters for Energy Utilization Enhancement

Ying Pang, *Member, IEEE*, Yanju Ji, Xinhao Zhang, Yongji Zhu, Gang Li, *Member, IEEE*, Cheng Gong, *Member, IEEE*, Zeng Xiang, *Member, IEEE*, Rong Han, *Member, IEEE*, Haigen Zhou, *Member, IEEE*, Man-Chung Wong, *Senior Member, IEEE*, and Jun Lin

***Abstract*—Due to the extremely limited source capacity of the automobile-based electromagnetic prospecting transmitters, their energy utilization is very important. The impedance matching technology can raise energy utilization by solving the reactive power. However, the impedance matching technology under nonlinear square-wave voltages has seldom received attention. Until now, no paper has pointed out how to solve the contradiction between the ideal control objective and the dc voltage hardware limitation. Thus, this article focuses on energy utilization improvement through impedance matching, especially for nonlinear square-wave voltages. First, an injection circuit coupling impedance matching converter (ICMC) is proposed as the basement. Then, to deal with the above contradiction, a compromised weight gain is defined to describe the degree of compromise with dc voltage limitations. Third, the compromised matching reference current optimization calculation method can balance the dc voltage requirement and raise the signal-to-noise ratio. Fourth, a control method is proposed to realize the matching reference current. Finally, the comparative experimental hardware results show the ICMC realizes 31.0%–65.5% larger current amplitude improvement with per-unit dc voltage compared to previous methods due to the optimized distribution of more capacity in the compensation for the frequency order with more serious SNR issues.**

***Index Terms*—Electromagnetic method (EM), geological prospecting, injection circuit, nonlinear voltage, reactive power compensation.**

Received 11 September 2024; revised 28 November 2024; accepted 11 December 2024. Date of publication 16 December 2024; date of current version 28 January 2025. This work was supported in part by the National Natural Science Foundation of China under Grant 42030104, in part by Science and Technology Development Plan Project of Jilin Province, China, under Grant 20240602061RC, in part by Special Financial Grant from the China Postdoctoral Science Foundation under Grant 2023TQ0132, in part by Outstanding Youth Program from the Education Department of Jilin Province under Grant JJKH20241279KJ, in part by Open Research Project from the Key Laboratory of Geophysical Exploration Equipment under Grant GEIOF20230101, in part by International Postdoctoral Exchange Fellowship Program (Talent-Introduction Program) under Grant YJ20220403, in part by the State Key Laboratory of Internet of Things for Smart Cities of the University of Macau under Project 001/2024/SKL, in part by the Macau Science and Technology Fund, Macau SAR, under Grant FDCT0017/2022/A1 and Grant FDCT 0003/2020/AKP, and in part by the Research Committee of the University of Macau under Grant MYRG2022-00035-FST and Grant MYRG-GRG2023-00044-FST. Recommended for publication by Associate Editor J. Biela. *(Corresponding authors: Gang Li; Jun Lin.)*

Ying Pang, Yanju Ji, Xinhao Zhang, Yongji Zhu, Gang Li, Haigen Zhou, and Jun Lin are with the Key Laboratory of Geophysical Exploration Equipment, Ministry of Education, Jilin University, Changchun 130021, China, and also with the College of Instrumentation and Electrical Engineering, Jilin University, Changchun 130021, China (e-mail: pangying@jlu.edu.cn; jiyj@jlu.edu.cn; xinhaoz22@mails.jlu.edu.cn; ligang2013@jlu.edu.cn; zhouhaigen@jlu.edu.cn; lin_jun@jlu.edu.cn).

Cheng Gong is with the State Key Laboratory of Analog and Mixed-Signal VLSI, University of Macau, Macao 999078, China, also with the Institute of Microelectronics, University of Macau, Macao 999078, China, and also with the Department of Electrical and Computer Engineering, Faculty of Science and Technology, University of Macau, Macao 999078, China (e-mail: cgong@um.edu.mo).

Zeng Xiang is with the Aerospace Yinshan Electric Company Ltd., Zhuhai 519000, China (e-mail: yb57435@um.edu.mo).

Rong Han is with the School of Optoelectronic Engineering and Instrumentation Science, Dalian University of Technology, Dalian 116024, China (e-mail: hanrong@dlut.edu.cn).

Man-Chung Wong is with the State Key Laboratory of Internet of Things for Smart City, University of Macau, Macao 999078, China, also with the State Key Laboratory of Analog and Mixed-Signal VLSI, University of Macau, Macao 999078, China, and also with the Department of Electrical and Computer Engineering, Faculty of Science and Technology, University of Macau, Macao 999078, China (e-mail: mcwong@um.edu.mo).

Color versions of one or more figures in this article are available at https://doi.org/10.1109/TPEL.2024.3518486.

Digital Object Identifier 10.1109/TPEL.2024.3518486

NOMENCLATURE

A. Abbreviations

EM	Electromagnetic method.
IGBT	Insulate-gate bipolar transistor.
TCLC	Thyristor control inductor and capacitor.
ICMC	Proposed injection circuit coupling impedance matching converter.
PWM	Pulsewidth modulation.
SNR	Signal-to-noise ratio.
KVL	Kirchhoff's voltage law.
FFT	Fast Fourier transform.
DSP	Digital signal processor

B. Symbols

Structure of ICMC Referred to Fig. 1

D_1–D_4	Diodes 1–4 of the rectifier.
T_1– T_4	IGBT 1– 4 of the transmitter.
G_1– G_4	IGBT 1– 4 of the ICMC H-bridge.
C_{dct}, C_{dcc}	Dc capacitor of rectifier and ICMC.

L_w, R_w	Inductance and resistance of antenna
R_L, C_L	Resistance and capacitance of the earth.
X_L, R_L	Equivalent inductive reactance and resistance of the antenna and earth combination.
T_p, C_p, L_p, and L_c	Transformer, capacitor, and inductor components of the injection circuit coupling of ICMC and ICMC output inductor.
Mp	Transformation ratio between load side and the ICMC side of the ICMC transformer.
X_{Lcn}	Impedance of L_c at the nth-order frequency.
Control Parameters	
f, n	subscripts are fundamental frequency and nth-order frequency components of signals.
$*$, $\#$	Superscripts are reference signals and ideal results signals.
v_s, v_L	Source voltage and load voltage, respectively
i_c, i_c^*	Injecting current and injecting current reference, respectively.
i_L, i_{Ln}	Load current, the nth-order FFT component of load current, respectively.
S, S_c, $S_{\max}$	Operating capacity, injecting capacity, and maximum capacity of the ICMC, respectively.
SNR_{iLn}	SNR of load current at nth-order frequency.
$\mathrm{SNR}_{iLn}^{\#}$	Ideal SNR value of nth-order frequency component after impedance matching.
SNR_{Cn}^{*}	Compromised SNR value of nth-order frequency component after impedance matching.
W_C	Set of compromised weights.
W_{Cn}	Compromised weight at nth-order frequency.
V_{MP}, V_{MP1}	Transformer voltage of the load side and the ICMC side, respectively.
$V_{\mathrm{dc}\,c}$, V_{inv}	Dc voltage and inverter voltages of ICMC, respectively.
X_{Lcn}	Impedance of ICMC output inductor at the nth-order frequency
I_{noin}	Amplitude of the noise at nth-order frequency.

I. Introduction

CURRENTLY, the vast majority of reactive power compensation studies are carried out under sinusoidal voltages of the grid. However, some special applications under nonsinusoidal and nonlinear voltages also require reactive power compensation to improve the capacity utilization of the source [1]. Reactive power compensation at nonlinear, nonsinusoidal voltages is still seldom understudied [2]. Among the applications under nonsinusoidal and nonlinear voltages, the EM geological prospecting system is one of the typical systems operating under nonlinear square wave voltage with frequency variations

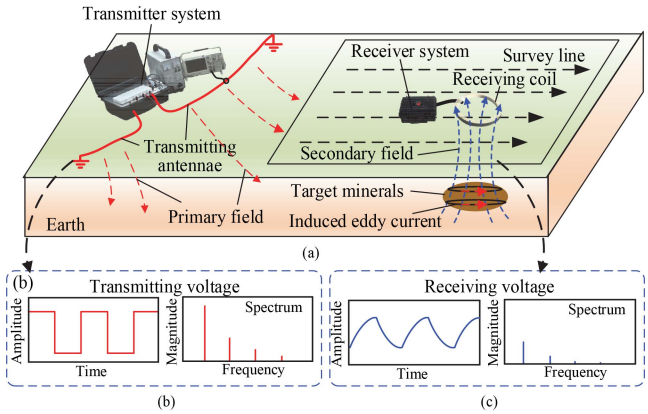

Fig. 1. (a) Schematic of the electromagnetic detection system, including transmitter system and receiver system, (b) the transmitting voltage waveform and its spectrum, and (c) the receiving current waveform and its spectrum.

[3]. The automobile-based EM geological prospecting system can explore underground mineral and oil resources, which are important for a country's development [4]. EM prospecting is a geological prospecting method of detecting underground conditions by adding voltage to the antenna and the earth and detecting the return current. With a larger return current amplitude, the prospecting results can be obtained more accurately [5]. Because of the attenuation of the prospecting signal as it travels deeper into the ground, the output power of the source must be continuously increased in order to obtain a larger value of the prospecting current and, finally, to obtain a clearer and more accurate return signal [6].

The schematic of the electromagnetic detection system, including the transmitter system, receiver system, and signal processing parts, is shown in Fig. 1(a). The electromagnetic prospecting system is usually composed of a transmitter system and a receiver system. The transmitting system is responsible for outputting a voltage of a specified waveform into the antenna, the receiving system is responsible for receiving the signals returned after propagation through the antenna, and the signal processing system processes the received signals into an image containing information about the subsurface geology. These systems are introduced as follows separately.

1) The transmitter system consists of the transmitting antennas that generate primary electromagnetic signals. First, the transmitter system injects square-wave voltage into transmitting antennas and earth load. Then, as shown in Fig. 1(b). Then, the ac square-wave voltage causes electromagnetic induction and radiates a primary electromagnetic wave field into underground space [5].
2) The receiver system integrated with receiving coils is placed in the survey area for electromagnetic signal collection. After the primary electromagnetic wave field arrives at the target underground area, the induced eddy current is produced. Then, induced eddy currents can further cause secondary fields. As the secondary fields pass through the receiving coil, Due to the principle of electromagnetic induction, an induced current is generated in the receiving coil as Fig. 1(c).

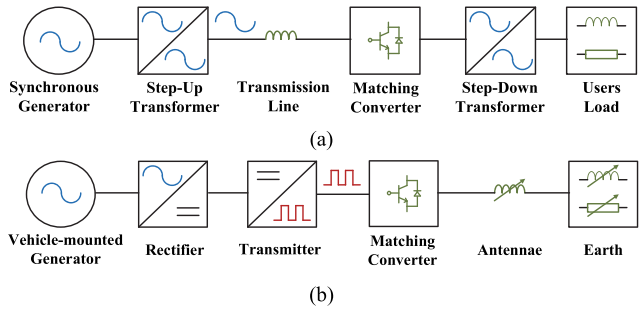

Fig. 2. Comparison between impedance matching technology in (a) sinusoidal voltage grid system, and (b) Nonlinear square wave volage geological prospecting system.

3) Based on the actual electromagnetic signals received, the signal processing part can invert the underground geological structure and the physical parameters of the target area (e.g., resistivity and dielectric constant) based on the relevant algorithms in the geological field [8]. Commonly used algorithms include the least squares method and conjugate gradient method.

In practical application, there are two factors that prevent the increase of output power at the source. 1) Unlike the grid system shown in Fig. 2(a), the EM geological prospecting system, as shown in Fig. 2(b) is an OFF-grid system powered by an automobile-based generator, which has limitations in terms of power supply as well as size and weight [7]; 2) Unlike impedance matching devices that take up the capacity of the generating side with reactive power caused by inductance on the transmission lines in pairs in the grid, there are as yet no solutions in EM geological prospecting system under nonlinear square wave voltage with variable load (determined by the antenna and the earth location) [8].

Previously, scholars have identified the problem of reactive power occupation of sources in the sinusoidal power grid and proposed a series of solutions, as follows [9], [10], [11], [12], [13], [14]. In the beginning, the series resonance principle is applied in Fig. 2(a) in the grid transmission line to eliminate the reactance. A fixed passive impedance network composed of the capacitor and inductor is connected in series with the transmission to compensate for the reactive caused by the line inductance on transmission lines [9]. Based on the principle of resonance, He et al. [10] set the control objective of the impedance of the converter to be the resonance value at the needed frequency to increase the current at the corresponding order. The inductive reactance of the internal resistance of the synchronous generator also gives rise to the problem of reduced generator output efficiency [11]. Naderi et al. [12] developed converters that resonate the impedance matching converter with the generator's internal resistance to maximize the power transmitted by the generator to the grid. Similar to grid applications, impedance matching converters have been developed for the sinusoidal current power amplifiers, where the control objective is the opposite of the load inductive reactance, thus solving the problem of low efficiency due to reactive power occupation [13], [14].

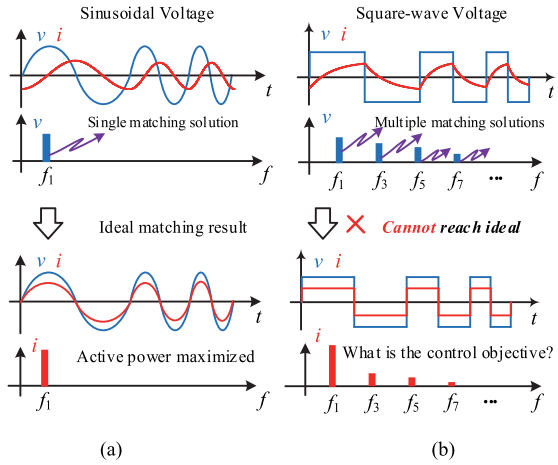

Fig. 3. Comparison of Impedance matching solution between (a) linear conditions before matching, (b) nonlinear conditions after matching and its dilemma.

The impedance matching under linear sinusoidal voltages [9], [10], [11], [12], [13], [14] has one unique control objective due to sinusoidal voltages having only a fixed frequency spectrum, as Fig. 3(a) shows. If the impedance of the impedance matching converter can be controlled to this unique control objective, the power utilization of the power source can be optimized to maximum. The unique control objective is the ideal impedance matching solution. Unlike the solution under linear sinusoidal voltage, the ideal impedance matching solution under square-wave voltage is a superposition of solutions at infinite frequency components. According to Fourier decomposition, the square-wave voltage yields an infinite number of frequency components, each of which corresponds to an impedance matching solution, as shown in Fig. 3(b). Fig. 3(b) also demonstrates the dilemma of impedance matching at square wave voltages. The dilemma is that the ideal matching target is unattainable, and a balance needs to be made between the ideal effect and the actual hardware to determine the control target.

However, in practice, impedance matching converters are limited by hardware parameters and capacity and cannot fully realize the ideal control objective of the infinite number of frequency components, i.e., the ideal reactive power control objective of compensating is to match the current as a square wave. For the problem of not being able to determine an ideal solution under square-wave voltage, researchers have used different algorithms to find control objectives that approximate ideal values. Pang et al. [2] applied two TCLC branches to compensate only the fundamental and third-order frequency components, respectively, for accessing the approximate compensation result. Zhou et al. [15] proposed a method of approximating the results through multiple trials and errors, where several different compensation attempts are made to select one of the better results as the ideal matching solution. Wang et al. [16] proposed to form a look-up table of control targets based on the data parameters such as temperature, frequency, voltage, and current waveforms correspondingly in advance. The look-up table determines the control objective according to actual measured values [16]. Huang et al. [17] and Li et al. [18] proposed a method to calculate the reactive power approximation only considering the first- to

TABLE I
CHARACTERISTIC COMPARISON AMONG DIFFERENT IMPEDANCE MATCHING CIRCUIT AND ITS CONTROL

Year	2021	2021	2023	2024	2021	2022	2024
Reference	[9], [10]	[11], [12]	[13], [14]	[2], [15]	[16]	[17], [18]	This article
Voltage waveform	Linear sinusoidal			Non-linear (also can be applies to linear sinusoidal)			
Matching purpose	Minimized reactive power consumption of source	Minimized reactive power consumption of source	Minimized internal resistance sum of the load and source	Minimized reactive power consumption of source	Minimized reactive power consumption of source	Minimized the amplitude of harmonics	Minimized reactive power consumption of source
Converter impedance objective value	Opposite to the load impedance value in fundamental frequency	Opposite to the load impedance value in fundamental frequency	Impedance and power supply internal resistance and minimum	Choose the better of the two by trial and error	Selection based on empirical values by checking the table after sampling	Resonance value of the corresponding harmonic	Adaptive search for optimality through theoretical modelling
Is there a unique solution?	Unique solution with single control objective is determined under linear single frequency			Multiple solutions with different objectives under complex spectra			
Is reactive power compensated at multiple frequency points?	No	No	No	Yes	No	No	Yes

**Note*: Shaded areas indicate corresponding weaknesses or inapplicability to the environmental characteristics of the applications.

forth-order frequencies of a square wave voltage as a control objective for reactive power compensation under square wave voltage.

In order to compare the characteristics of the various methods, the calculation method, and topology of the impedance matching control objectives in the above literature are summarized in Table I. As [9], [10], [11], [12], [13], and [14] are impedance matching under sinusoidal voltages. As [15], [16], [17], [18] are impedance matching under square wave voltages. Based on the above literature review and the comparative analysis in Table I, the authors found that there is still no reference calculation algorithm for impedance matching research on square wave voltage. The reference calculation algorithm needs to point out how the control objective can be determined to achieve the maximumly optimized impedance matching result with the consideration of hardware limitation from a theoretical point of view.

Therefore, this article extends the impedance matching control objective theoretical calculation method from only in linear sinusoidal systems to nonlinear square-wave systems. Then, this article proposes an ICMC with its control method to realize the proposed matching reference current. The detailed contributions are provided as follows.

1) The reason that the ideal control objective cannot be reached is explained by the contradiction between the unrealizable ideal control objective and the dc voltage hardware limitation in the impedance matching under non-linear square-wave voltages for the first time.
2) A compromised weight gain is defined to describe the degree of compromise of the reference waveform, first considering hardware limitations in the impedance matching area.
3) Based on the compromised weight gain, a compromised ideal matching reference current calculation method that is explored. Then, the compromised ideal matching reference current can ensure the maximumly optimized impedance matching result under current dc voltage hardware conditions by the proposed control method.
4) A transformer-coupled impedance matching topology ICMC is created. By the injected structure constituted by the coupled transformer, the proposed reference current can be injected into the system to realize the impedance matching effect.

In summary, this article can guide users in solving reactive power occupancy problems caused by the load characteristics without increasing the transmitter capacity under special nonlinear square-wave voltage. The rest of this article is organized as follows. Section II gives the details of the proposed ICMC impedance matching topology. In Section III, the optimization goal in square-wave voltage impedance matching and a compromised weight gain based on the optimization goal are defined for solving the contradiction between the unrealizable ideal control objective and the dc voltage hardware limitation. Next, the compromised ideal impedance matching reference current calculation method are introduced to lay the theoretical foundations of impedance matching under square waves. And its control method to achieve the above compromised calculation method is presented in Section IV. Then, a comparative hardware experimental testing platform is built to express the hardware experimental results in Section V. Finally, Section VI concludes this article.

II. PROPOSED ICMC IMPEDANCE MATCHING TOPOLOGY

Fig. 4 introduces the circuit configuration of the EM transmitter, load, and the proposed ICMC EM impedance matching system. The generator and diodes D_1– D_4 of the rectifier make up the dc power supply of the transmitter. The transmitter is composed of four controllable IGBTs T_1– T_4 and a dc capacitor $C_{\mathrm{dc}t}$ to generate the special nonlinear square-wave voltage for the purpose of EM geological prospecting. Linear voltage means that the voltage rises or falls continuously (sinusoidal is continuous), and nonlinear means that there are abrupt or step changes in voltage. Compared to the single-frequency sinusoidal voltage used in distribution grids, the square voltage adopted in electromagnetic detection is a typical nonlinear signal, as it has periodic step changes. At the voltage jump points, the left-hand limit is not equal to the right-hand limit The antenna (L_w and R_w) and the earth (R_{L1}, R_{L2}, and C_L) consist of the

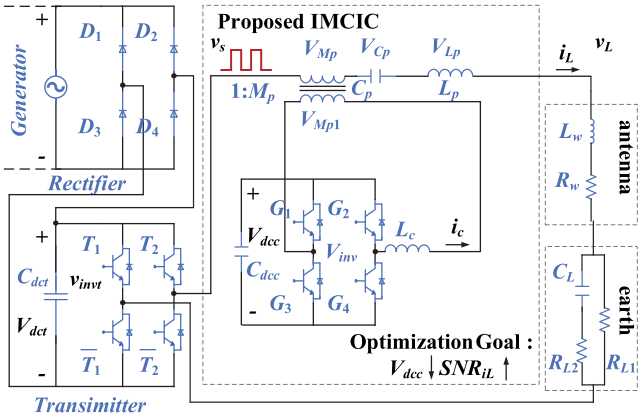

Fig. 4. EM transmitter, load, and proposed ICMC circuit configurations.

load of the EM system. v_s, v_L stands for the output voltage of the transmitter and the voltage between the load. Suppose there is no impedance matching system $v_s = v_L$. If the impedance matching system is added $v_s \neq v_L$, the impedance matching system can be considered as a controllable voltage source and equally to change the voltage between the load.

The proposed ICMC circuit configuration is composed of 1) the current injection coupling part and 2) an active current-producing part. The current injection coupling part consists of transformer T_p, capacitor C_p, and inductor L_p, which is used to inject current and coupled with the main circuit of the EM system. C_p and L_p can reduce the dc voltage requirement for fundamental frequency compensated power. C_p can be designed by

$$C_p = \left[(2\pi f)^2 \cdot L_W\right]^{-1} \tag{1}$$

where L_w is difficult to accurately estimate by using a DSP-based power electronic inverter control system [19]. The inductance of an antenna is not fixed, and its inductance value may vary significantly during different detections. The common inductance range is from 1 mH to 20 mH [2]. Therefore, the wide variation range of L_w causes difficulty in estimating to some degree [7]. Additionally, the accurate measurement of L_w inductance requires a complex process and equipment. The complex measurement process is difficult to realize for the DSP-based control system of active current-producing part. The active current-producing part is formed of a single-phase full H-bridge. The single-phase full H-bridge is composed of four IGBTs G_1– G_4 and a parallel dc capacitor $C_{\mathrm{dc}c}$. Through the PWM control, the H-bridge can produce the injecting current i_c following the reference current $i_c = i_c^*$. i_c can inject into the main EM system through the current injection coupling part. The calculation process of i_c^* is going to be presented in Section IV-A.

III. Optimization Goals and Compromised Weight

In this section, for the purposes of laying the theoretical foundations of impedance matching under square waves, the basic constraints and optimization goals for the EM geological prospecting system are given in Section III-A. Then, a compromised weight gain is defined to describe the degree of compromise of the reference waveform in Section III-B. Third, the relationship between compromised weight and operating parameters is given in Section III-C.

Algorithm I: Compromise Ideal Reference Current Calculation Method.

Input:
- Sampling source voltage v_s, load current i_L, ICMC DC voltage V_{dcc};
- Range of ICMC DC voltage $[V_{dcc(\min)}, V_{dcc(\max)}]$;
- Noise thresholds $i_{\mathrm{noi}n}$;

1: FFT analysis of v_s and i_L.
2: Calculate the required SNR of all frequency order based on (18) and FFT;
3: Determine the compromise weight W_C by EM geological prospecting requirements and (19).
4: Update the set of compromise weight W_C by (9).
5: Calculate the reference SNR at each frequency order by (20);
6: Calculate the reference current i_{Ln}^* by (21);
7: Verify whether the required DC satisfy the $[V_{dcc(\min)}, V_{dcc(\max)}]$ by (13) and (15).
8: **If** yes end for,
else initialize a series and assign $\Delta W_C + W_C \rightarrow W_C$, then Verify whether the required DC;
If yes calculate a series updated SNR_{iLn}^* by (20);
Compare SNR_{iLn}^* and select the largest one;
Output corresponding i_{Ln}^*;
else initialize another series of $\Delta W_C + W_C$;

Output: reference current i_{Ln}^*.

A. Constraints and Optimization Goals

In the application scenario of the EM geological prospecting system, the current amplitude at each frequency point implies the clarity of the prospecting result. Only when the current amplitude is higher than the noise thresholds can it be considered a valid prospecting signal, as shown in Fig. 5(c). A higher SNR means higher prospecting clarity [20]. Therefore, the primary optimization goal of impedance matching in EM is maximizing the SNR at each frequency order as the optimization goal of (2). The proposed impedance matching system can increase the amplitude of the current. As shown in Fig. 6(a), different amounts of compensation at different nth-order frequency points correspond to different SNR results SNR_{iLn}. At the same time, higher compensating frequencies and higher compensation current amounts lead to higher dc voltage $V_{\mathrm{dc}c}$ demands, as shown in Fig. 6(b), where the peripheral cubes represent higher dc voltage ($V_{\mathrm{dc}c2} > V_{\mathrm{dc}c1}$) demands due to higher compensation frequencies and compensation currents compared to the internal cubes.

Thus, impedance matching systems for EM geological prospecting systems cannot compensate for reactive power without limitations. There are some constraints during operations. The constraints include 1) current amplitude at corresponding

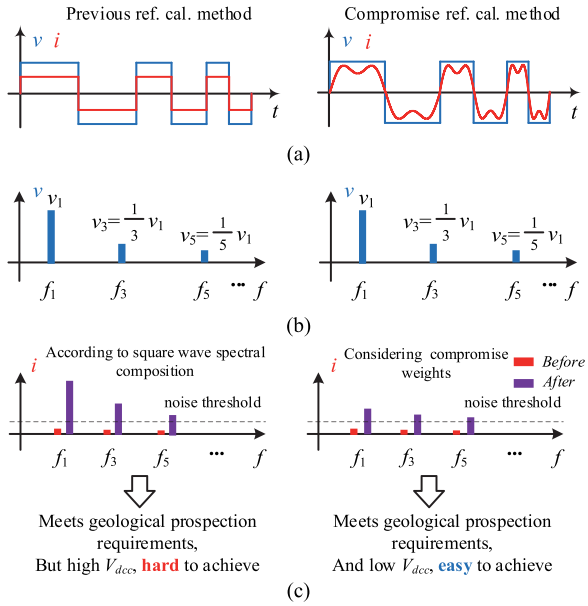

Fig. 5. Comparison between previous method and the proposed compromise reference calculation method in (a) time domain, (b) frequency domain of voltage, and (c) frequency domain of current.

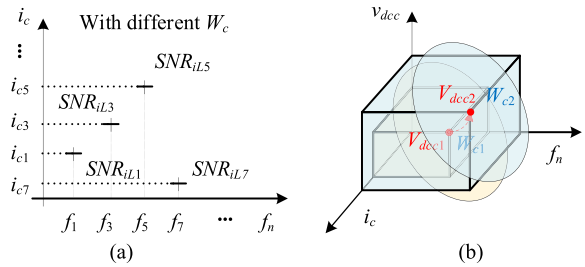

Fig. 6. Relationship among compensating current amount i_c, compensating frequency f_n with different compromise weight W_C, resulting in (a) different SNR and (b) required dc voltage after compensation.

n-order frequency $\{ i_{L1}, i_{L2}, \ldots, i_{Ln}\}$, 2) SNR of the current at the corresponding n-order frequency $\{ \mathrm{SNR}i_{L1}, \mathrm{SNR}i_{L2}, \ldots, \mathrm{SNR}i_{Ln}\}$, 3) the operating dc voltage of the ICMC $V_{\mathrm{dc}c}$, and 4) the total capacity S of the ICMC [21]. For the purpose of obtaining clear prospecting results, the typical constraints and multiobjective optimization problem of the EM geological prospecting system can be stated as

$$\begin{aligned} \text{maximum} \quad & \mathrm{SNR}i_{Ln} = [\mathrm{SNR}i_{L1}, \mathrm{SNR}i_{L2}, \ldots, \mathrm{SNR}i_{Ln}] \\ \text{subject to} \quad & V_{\mathrm{dc}c} < V_{\mathrm{dc}c\max} \\ & I_{Ln} > 0, n = 1, 2, 3 \ldots \\ & S < S_{\max} \end{aligned} \tag{2}$$

where $V_{\mathrm{dc}c\max}$ is the designed maximum dc voltage of ICMC, and $S_{\max}$ is the designed maximum capacity of ICMC. $V_{\mathrm{dc}c\max}$ and $S_{\max}$ are determined after the ICMC is designed and manufactured. Here, the goal is to maximize the objective vector $\mathrm{SNR}i_{Ln}$, which contains n scalar objectives and is subject to three different inequality constraints. The l-2 norm of SNR_{iLn} can be calculated by (3) as a way to evaluate the optimization process

$$\|\mathrm{SNR}_{iLn}\|_2 = \sqrt{\mathrm{SNR}_{iL1}^2 + \mathrm{SNR}_{iL2}^2 + \cdots + \mathrm{SNR}_{iLn}^2}. \tag{3}$$

Obviously, when the vector SNR_{iLn} is optimized to the global optimal solution, the l-2 norm of vector SNR_{iLn} reaches its maximum. The specific meaning of maximum (3) is that the SNR of the detecting current $\mathrm{i_{Ln}}$ at each frequency order reaches its maximum. In this article, the optimization of SNR_{iLn} is influenced by multiple constraints, including the capacity of ICMC, the dc voltage of ICMC $V_{\mathrm{dc}c}$, compensating current amplitude, and frequency order i_{cn}. In addition, vector SNR_{iLn} is composed of n components. The optimization problem of vector SNR is a multiobjective optimization problem. Therefore, the SNR_{iLn} optimization problem in this article is a multiobjective optimization problem influenced by multiple factors. For example, if the final optimization limits the specific SNR_{iLn} at a certain frequency point, the optimization result will be different. Furthermore, the optimization results under different constraints are also different. Thus, in Section IV of this article, a common operating condition of electromagnetic prospecting transmitters is provided as the constraint. The specific constraint given in Section IV is to achieve the lowest operating voltage $V_{\mathrm{dc}c}$ while ensuring that the SNR_{iLn} ratio of each frequency point meets the requirements. Due to the injecting current i_{Ln} being limited by $V_{\mathrm{dc}c}$ through (13), the l-2 norm is maximum with the specific constraint given in Section IV.

Additionally, when the following conditions are limited, the multiobjective optimization problem in this article can be considered as a convex optimization problem. If only considering maximizing the SNR of a single frequency point, it can be transformed into a convex optimization problem. After multiple constraints are determined, such as ICMC dc voltage $V_{\mathrm{dc}c}$, ICMC system capacity $S_{\max}$, the optimization problem in this article can be considered as a convex optimization problem.

The optimization process described above is to obtain the highest SNR of the detected signal. Because the SNR at different frequency order SNR_{iLn} reflects the clarity of the results at different depths, (2) is a multiobjective optimization problem. Unlike single-objective problems, the concrete optimization goal for each SNR_{iLn} of optimality in multiobjective optimization problems is not evident. In fact, SNR_{iLn} has no single global optimal solution for such problems. Therefore, another constraint must be defined to specify the optimal solution. This article defines a metric called compromised weight to balance the contradiction between the matching result and the dc voltage, as shown below.

B. Compromised Weight

Theoretically, the ideal matching result is shown in Fig. 3(b), but this result is not achievable in practice. The reason is that this matching result requires a larger energy to be provided at each frequency point, as shown in Fig. 5. Ultimately, it would require the entire system to provide at very high reactive power and operate with very high dc voltage far beyond the transmitter system, as shown in Fig. 6(b). In the ideal condition, the $\mathrm{v_{RL}}$

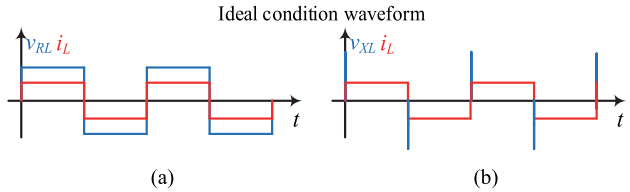

Fig. 7. (a) v_L voltage and i_L current waveform in ideal condition, and (b) v_{XL} voltage and i_L current waveform in ideal condition.

voltage and i_L current waveforms are shown in Fig. 7(a). Based on Fig. 7(a), in the ideal condition, the load current amplitude reaches the maximum value as (4). The ideal load current is a square waveform as (5)

$$I_{L\max} = \frac{V_s}{R_L} \tag{4}$$

$$i_{Lideal} = \begin{cases} I_{L\max}, nT \le t < nT + 0.5T \\ -I_{L\max}, nT + 0.5T \le t < (n+1)T \end{cases} \tag{5}$$

Then, based on (4) and (5), the voltage on the equivalent X_L can be calculated as

$$\begin{aligned} v_{XLideal} &= L\frac{di_{Lideal}}{dt} \\ &= 2L \cdot I_{L\max}\delta(t) - 2L \cdot I_{L\max}\delta(t + 0.5T) \end{aligned} \tag{6}$$

where τ is the pulse width. δ(t) is the Dirac δ-function. $v_{XLideal}$ is a pulse waveform with a pulse width that tends to 0. Further combining the voltage relationship in Fig. 7, the voltage to be supplied by the ICMC part can be solved as

$$\begin{aligned} v_{ICMC} &= v_s - v_{XLideal} - v_{RL} = -v_{XLideal} \\ &= -2L \cdot I_{L\max}\delta(t) + 2L \cdot I_{L\max}\delta(t + 0.5T). \end{aligned} \tag{7}$$

Based on (7), the required voltage for ICMC is also a pulse voltage with a pulse width that tends to 0. Structurally, the ICMC is a special H-bridge structure coupled to the system via a transformer. Theoretically, it is possible to realize the pulse voltage injection of (7). However, in reality, all parts of the circuit have internal resistance and output inductance, and injecting an ideal pulse voltage is not possible, which requires an infinite amount of V_{dcc} and energy to overcome the effects of internal resistance and inductance. Therefore, the compromised weight W_{Cn} for the nth-order frequency component is defined as (8) to solve the problem

$$\mathrm{SNR}_{CiLn} = (1 - W_{Cn}) \cdot \mathrm{SNR}^{\#}_{iLn}, 0 \le W_{Cn} \le 1 \tag{8}$$

where $\mathrm{SNR}^{\#}_{iLn}$ is the ideal SNR value of the nth-order frequency component after impedance matching. SNR^{*}_{Cn} is the compromised SNR value of the nth-order frequency component after impedance matching. W_{Cn} characterizes the degree of compromise. The lower the degree of compromise, the closer the compromised impedance match is to the ideal value SNR^{*}_{n}. Thus, the compromised weight W_C is the set of n compromised weights W_{Cn} at the nth-order frequency component, as shown in (9). The degree of compromise at each frequency W_{Cn} collectively makes up the overall degree of compromise for the entire system W_C

$$W_C = \{W_{C1}, W_{C2}, \ldots, W_{Cn},\}. \tag{9}$$

The compromised weights W_C of the system are determined by a combination of the constraints of the system's operating conditions and the needs of the detection goal. If the compromised weights are to be determined, the limitations of the system's operating conditions and the detection target requirements are first needed in relation to the compromised weights. This relationship is presented in Section III-C.

C. Relationship Between Compromise Weight and Operating Parameters

Because the compromised weight W_C reflects how close the actual matching result is to the ideal matching result. Therefore, the closer the matching result is to the ideal one, the higher the requirements on the operating parameters of the matching system will be, including the operating dc voltage V_{dcc}, the number of matched frequency points n, the voltage V_{Lp} between coupling inductor L_{pf} the amplitude of the load current i_L. The location of operating parameters in the system is shown in Fig. 4. The trend relationship between changes in operating parameters and compromised weights can be expressed by

$$V_{\mathrm{dcc}} \propto (1 - W_{Cn}), V_{Lpf} \propto (1 - W_{Cn}), i_L \propto (1 - W_{Cn}). \tag{10}$$

Equation (10) represents the trend relationship. Assuming the ideal voltage between the load after impedance matched is $V^{\#}_{Ln}$. The specific calculations for each operating parameter can be obtained by comparing the ideal matching results. The inverter output voltage V_{MP1} has a relationship with $V^{\#}_{Ln}$ as (12). In other words, if V_{MP1} can be controlled as (11), the voltage between loads can be controlled equal to the ideal matching result $V^{\#}_{Ln}$

$$V_{Mp1n} \to V^{\#}_{Mp1n} \Rightarrow V_{Ln} \to V^{\#}_{Ln} \tag{11}$$

$$V^{\#}_{Mp1n} = V_{sn} - V^{\#}_{Ln} - V_{Cpn} - V_{Lpn} \tag{12}$$

where V^{*}_{Ln} is the reference voltage between the whole load side. In addition, V_{MP1} can be calculated using circuit KVL theory (13), which consists of fundamental voltage V_{invf} and harmonic voltage V_{invf}

$$\begin{aligned} V_{Mp1} = M_p \cdot V_{Mp} &= \sqrt{V^2_{invf} + V^2_{invh}} \\ &+ \sqrt{(I_{cf}X_{Lcf})^2 + \sum\nolimits_{n=2}^{\infty} I^2_{cn}X^2_{Lcn}} \end{aligned} \tag{13}$$

where V_{MP} is the transformer voltage coupling on the load side. Mp is the transformation ratio between the converter side and the circuit coupling side. X_{Lcf} is the impedance of L_c at the fundamental frequency, and X_{Lcn} is the impedance of L_c at nth-order frequency. The impedance of L_c can be calculated as

$$X_{Lcf} = 2\pi f \cdot L_c, X_{Lcf} = 2\pi nf \cdot L_c \tag{14}$$

where the fundamental frequency f is selected as 50 Hz. In actual usage, the fundamental frequency can be chosen as another

value for calculation convenience. The minimum requirement of operating dc voltage $V_{\mathrm{dc}c}$ is

$$V_{\mathrm{dcc}} \geq \sqrt{2} \cdot \sqrt{V_{invf}^2 + V_{invh}^2}. \tag{15}$$

Equations (12)–(15) show the relationship between compromised weight and operating dc voltage. Additionally, based on the above three (12)–(15), The current in the impedance matching system ICMC I_{cf} and I_{cn} can be jointly solved. Based on the limitations of operating dc voltage $V_{\mathrm{dc}c}$, the voltage V_{Lp} between coupling inductor L_{pf} can be deducted from [22]

$$V_{Lp} \leq V_{\mathrm{dcc}} = \sqrt{2} \cdot V_{Mp1}. \tag{16}$$

Because in the ideal matched result, the load side consisting of the antenna, the earth, and the impedance matching system can be considered purely resistive, the limitation of load current i_L can be calculated as

$$i_L \leq V_L \cdot \left(R_W + \frac{R_{L1} \cdot R_{L2}}{R_{L1} + R_{L2}} \right)^{-1}. \tag{17}$$

In summary, the operating parameters of the operating dc voltage $V_{\mathrm{dc}c}$, the voltage V_{Lp} between coupling inductor $L_{pf,}$ and the amplitude of the load current i_L can be, respectively, described as (15), (16), and (17).

IV. Compromised Impedance Matching Reference Current Calculation and Control Method

Based on compromised weight gain and the relationship between compromise weight and operating parameters, a compromised ideal impedance matching reference current calculation method is proposed in Section IV-A. Then, based on the compromised ideal impedance matching reference current calculation method, the overall compromised control method for the proposed ICMC is given in Section IV-B.

A. Compromised Ideal Reference Current Calculation Method

After the relationship between compromised weight and operating parameters has been figured out clearly, the conventional unrealizable ideal reference current can be considered to be replaced by a realizable compromised ideal reference current. The optimization goal can be set to meet the lowest SNR requirement to achieve the lowest energy loss as (2), or to achieve the highest SNR by achieving the highest power output as

$$\begin{aligned} \text{minimum} \quad & V_{Mp1} = M_p \cdot V_{Mp} = \sqrt{V_{invf}^2 + V_{invh}^2} \\ & + \sqrt{(I_{cf} X_{Lcf})^2 + \sum_{n=2}^{\infty} I_{cn}^2 X_{Lcn}^2} \\ \text{subject to} \quad & \mathrm{SNR}_{iLn}(x) > \mathrm{SNR}_{\mathrm{min}iLn}, n = 1, 2, 3 \ldots \\ & I_{Ln} > 0 \end{aligned} \tag{18}$$

where $\mathrm{SNR}_{\mathrm{min}iLn}$ is the minimum requirement of SNR at the corresponding nth-order frequency component. In practice, the user can choose one of the (2) or (18) optimization methods according to the needs of the application. The theory of the (2) and (18) optimization processes is the same. Only the values of the compromised weights are chosen differently. In the rest of this article, the optimization method shown in (18) has been chosen as an example design for the calculation of the reference current. Based on the optimization method of (18), the compromised ideal SNR_{iLn}^* at all frequency points is chosen as the minimum required $\mathrm{SNR}_{\mathrm{min}\,n}$, as shown in (19). Equation (19) also shows the relationship between the reference and compromised ideal SNR_{iLn}^* and the ideal $\mathrm{SNR}_{iLn}^{\#}$. Additionally, the delineation of SNR_{iLn}^* is given in (20)

$$\mathrm{SNR}_{iLn}^* = \mathrm{SNR}_{iLn}^{\#} \cdot W_{Cn} = \mathrm{SNR}_{\mathrm{min}\,n} \tag{19}$$

$$\mathrm{SNR}_{iLn}^* = 10 \lg \frac{i_{Ln}^*}{i_{\mathrm{noi}n}} \tag{20}$$

where $i_{\mathrm{noi}n}$ is the amplitude of the noise thresholds at the corresponding nth-order frequency component. Thus, the compromised ideal reference current i_{Ln}^* can be solved as (21) by substituting (19) into (20)

$$i_{Ln}^* = i_{\mathrm{noi}n} \cdot 10^{\frac{\mathrm{SNR}_{iLn}^*}{10}} = i_{\mathrm{noi}n} \cdot 10^{\frac{\mathrm{SNR}_{iLn}^{\#} \cdot W_{Cn}}{10}}. \tag{21}$$

In summary, the compromised ideal reference current calculation method is provided in Algorithm I. All of the conditions that Algorithm are needed to re-execute are summarized in Table II. When the dc voltage requirement is not met, the updated W_C can be computed by the iterative method. Due to W_C is initially calculated based on $[V_{\mathrm{dc}c(\mathrm{min})}, V_{\mathrm{dc}c(\mathrm{max})}]$, even if W_C does not meet the requirements, it will not be too far from the required range. Thus, the iterative method is suitable for W_c updating when the dc voltage requirement is not met.

After the critical reference current is determined, the impedance matching can be achieved at the theoretical level. With the noise thresholds at all frequency points taken as twice the peak noise. The proposed method is used to reasonably increase the SNR at each frequency point above the demanded SNR, which satisfies the detection requirements and reduces the dc voltage requirement as much as possible. Lower dc voltage can ensure an easier realization in the environment of geological prospecting without grid power.

In the following section, the implementation methodology impedance matching is provided from the aspects of the hardware topology and its control method.

TABLE II
Algorithm Re-Execution Conditions

Where does Change happen?	What intermediate variables are affected?	What variables are affected?
ICMC Hardware parameter	M_p, L_c, L_p, and C_p	Maximum i_c
ICMC operating parameter	V_{dcc}	Maximum i_c
Transmitter operating parameter	V_s, f	FFT of i_L
Ground characteristics	C_L, R_L	FFT of i_L
Weather significant changing	Noise level i_{noin}	SNR_{iLn}
Location significant changing	Noise level i_{noin}	SNR_{iLn}
Required SNR_{iLn} changes	SNR^*_{iLn}	SNR^*_{iLn}

B. Overall Control Method

After the compromised ideal impedance matching reference current i_L^* is calculated, a real injecting current i_c should be generated to finish the process of impedance matching. Thus, a supporting control strategy is going to be designed in this section. The supporting control strategy is divided into 1) injecting current reference i_c^* calculation and 2) IGBT controlling signals generation. Injecting current reference i_c^* is used as the reference signal for the PWM control to follow. Then, the current PWM method can generate the i_c close to i_c^* in real time. Thus, the calculation injecting current reference i_c^* is one of the critical steps in the control strategy. The calculation injecting current reference i_c^* is based on the compromised ideal impedance matching reference current i_{Ln}^*. After the i_{Ln}^* is obtained as (21), the reference voltage on the load can also be calculated as

$$v_L^* = \sum_{n=1}^{\infty} v_{Ln}^* = \sum_{n=1}^{\infty} i_{Ln}^* \cdot X_{Ln} \tag{22}$$

where n presents the needed matching order number. Users can choose the order number based on their requirements. Similarly, the reference voltage between the coupling C_p and L_p can also be deduced through (23) and (24), respectively, as follows:

$$v_{Cp}^* = \sum_{n=1}^{\infty} v_{Cpn} = \sum_{n=1}^{\infty} i_{Ln}^* \cdot X_{Cpn} \tag{23}$$

$$v_{Lp}^* = \sum_{n=1}^{\infty} v_{Lpn} = \sum_{n=1}^{\infty} i_{Ln}^* \cdot X_{Lpn} \tag{24}$$

where X_{Ln}, X_{Cpn}, and X_{Lpn} stand for the impedance of load, coupling C_p, and coupling L_p, respectively. They can be obtained from (25) and their corresponding series and parallel relationships

$$X_{Cpn} = (2\pi f n C_p)^{-1}, X_{Lpn} = 2\pi f n L_p. \tag{25}$$

Based on (11) and (12), the coupling transformer M_p can be considered as a controllable voltage source. The voltage between the M_p can be controlled to a voltage v_{MP1}^* to let the voltage between the load v_L close to the reference v_L^*. v_{MP1}^* is defined as the reference voltage of the transformer's primary side. v_{MP1}^* can be deduced by substituting (11) and (12) to (22)–(25) as

$$v_{Mp1}^* = v_s - v_L^* - v_{Cp}^* - v_{Lp}^*. \tag{26}$$

The ratio of the primary and secondary sides of the transformer can be used to control the voltage ratio of the primary and secondary sides, as in (27). And the ratio of the original and secondary sides can be designed according to the needs of the user in order to regulate the voltage $V_{\mathrm{dc}c}$ on the dc capacitor to meet the requirements in (2)

$$v_{Mp1} : v_{Mp} = 1 : M_p \tag{27}$$

where the v_{Mp} is the voltage of the transformer's secondary side. M_p is the transformer ratio and is selected as 1 in this article. The selection of M_p can optimize $V_{\mathrm{dc}c}$ at the design stage, which is a design optimization method. This article primarily concentrates on the optimization achieved through the control method. When optimizing $V_{\mathrm{dc}c}$ by changing M_p, the following points need to be noted.

1) For most transformers, the ratio is determined after manufacturing. Although there are a few transformers, the ratio can be adjusted. Adjusting the ratio in usage requires replacing the transformer or adjusting the hardware, which is very inconvenient.
2) Each component has the upper limitations for passing current. When the M_p is increased to reduce V_{dcc}, the current limitation should be noticed.
3) The rising slope of the injected current is determined by the dc voltage. When the $V_{\mathrm{dc}c}$ is reduced by increasing M_p, attention should be paid to ensuring the rising slope of the injected current.
4) The method of adjusting the ratio of the transformer amplifies the current and reduces the voltage for each frequency current energy.

Thus, the spectrum components of injecting power Sc do not change. The method is not effective when the operating conditions change. Based on (27), the reference voltage of the transformer secondary side v_{Mp}^* can be concluded as

$$v_{Mp}^* = M_p \cdot v_{Mp1}^* = M_p \cdot \left(v_s - v_L^* - v_{Cp}^* - v_{Lp}^*\right). \tag{28}$$

Also, there is a fixed proportionality between the current on the primary side and the current on the secondary side as in (29). Furthermore, the reference current i_c^* on the secondary side can be calculated as

$$i_L : i_c = M_p : 1 \Rightarrow i_c^* = i_L^* \cdot M_p^{-1}. \tag{29}$$

Based on (29) and the impedance of L_c, the reference voltage between L_c can be calculated as

$$v_{Lc}^* = \sum_{n=1}^{\infty} v_{Lcn}^* = \sum_{n=1}^{\infty} i_{cn}^* \cdot X_{Lcn} = \sum_{n=1}^{\infty} i_{cn}^* \cdot (2\pi f n L_c). \tag{30}$$

Finally, the reference voltage v_{inv}^* at the voltage output of the full H-bridge inverter can be calculated by combining (28) and (30) as

$$v_{inv}^* = v_{Lc}^* + v_{Mp1}^*. \tag{31}$$

Due to the output voltage of a full H-bridge inverter v_{inv} can be controlled close to the reference voltage v_{inv}^* through the voltage PWM method, e.g., space vector PWM and sinusoidal PWM. Based on the above reference voltage value v_{inv}^* and PWM method [23], the control system can control the proposed ICMC hardware system to generate the corresponding switching signals G_1–G_4 to complete the impedance matching. Next, comparative experiments will verify the feasibility of the hardware and control system proposed in this section.

V. Comparative Hardware Experimental Verifications

In this section, the viability and advantages of the proposed ICMC are verified through a group of hardware experimental comparisons. Pang et al. [2] and Tian et al. [14] are selected as the comparative group. The reasons for choosing [2] and [14] as the comparative are that 1) both [2] and [14] and the proposed

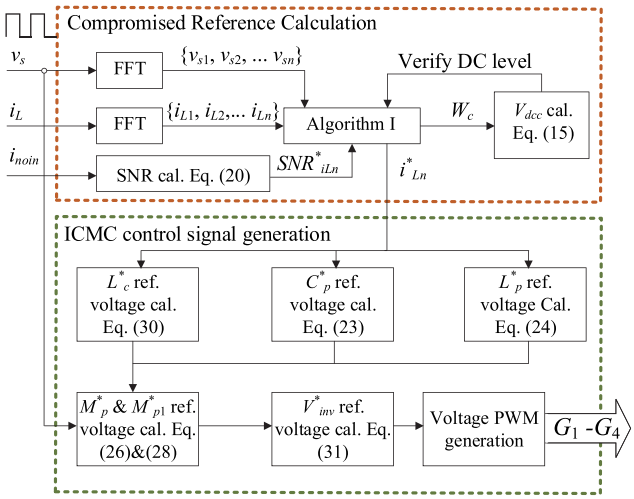

Fig. 8. Overall control flow chart of proposed control method.

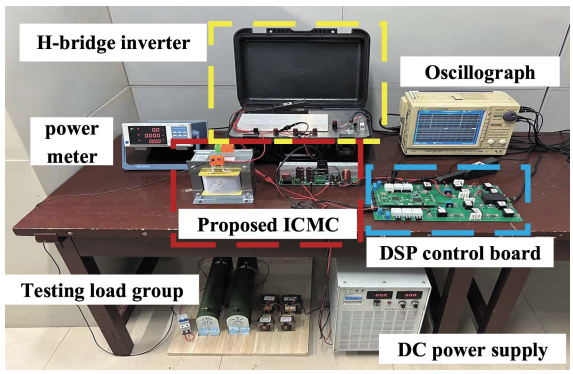

Fig. 9. Appearance of the proposed ICMC experimental prototype.

TABLE III
EXPERIMENTAL PARAMETERS SETTINGS

	Parameters	Physical values
Source voltage	V_s	±300 V
Nonlinear voltage fundamental frequency	f_1	100 Hz, 200 Hz, 300 Hz
Load	L_W, R_W, C_L, R_{L1}, R_{L2}	16 mH, 25 Ω, 10 μF, 5 Ω, 0.1 Ω
ICMC	L_c, C_P, L_P	3 mH, 180 μH, 0.4 μF

one use a full H-bridge to inject the compensating current; 2) both [2] and [14] and the proposed one apply a passive capacitor as the supplement of compensating reactive power to reduce the dc voltage of full H-bridge. Their differences are the selection of compensating reference current i_c^* and whether compensation for multiple frequency points is considered.

The experimental hardware platforms of the proposed ICMC and one of the state-of-the-art impedance matching converters in [14] are built, as shown in Fig. 9. The current reference calculation follows the proposed compromised ideal method in Algorithm I. The overall control diagram of the proposed ICMC is given in Fig. 8. The parameters in the experimental verifications are set in Table III. The SNR optimization results comparison between the proposed ICMC and previous methods are given in Table IV. The experimental results are summarized

TABLE IV
SNR RESULT COMPARISON BETWEEN PROPOSED ICMC AND PREVIOUS METHODS

Current amplitude and SNR			First-order		Third-order		Fifth-order		Seventh-order	
			i_{L1}** (A)	SNR_{iL1} (%)	i_{L3} (A)	SNR_{iL3} (%)	i_{L5} (A)	SNR_{iL5} (%)	i_{L7} (A)	SNR_{iL7} (%)
Without before matching			5.3	26.5	0.7	3.5	0.3	1.5	0.1	0.5
Previous* Maximum SNR method			8.5	42.5	1.7	11.0	0.94	8.5	0.55	6.0
Proposed optimization			6.0	30.0	2.8	14.0	1.6	8.0	1.2	6.0
Need V_{dcc}	Previous*	Each V_{dccn} (V)	350		350		350		350	
		Total $\sum V_{dccn}$ (V)	700							
	Proposed	Each V_{dccn} (V)	50		275		250		150	
		Total $\sum V_{dccn}$ (V)	400V (V_{dcc} reduces 42.9% SNR also satisfying)							

Note: "*" marks the matching method in [2] and [14].
"**" the current data in the table are rms values.

TABLE V
EXPERIMENTAL RESULTS COMPARISON WITH PREVIOUS METHODS

f_1	Compensating methods	$i_{Lp\text{-}p}$ (A)	P_s (W)	Q_s (Var)	V_{dcc} req. (V)	$i_{Lp\text{-}p}$ increasing (%)	$i_{Lp\text{-}p}$ increasing per V_{dc} (A/kV)
100Hz	Only fundamental	19.1	820	30	300	--	--
	With previous*	24.8	1006	18	700	29.8	14.3
	With proposed	32.2	987	21	400	68.6	65.5
200Hz	Only fundamental	18.9	890	35	300	--	--
	With previous*	22.6	1001	15	700	19.6	9.3
	With proposed	29.5	945	22	400	56.1	53.0
300Hz	Only fundamental	19.2	873	38	300	--	--
	With previous*	20.8	1012	18	700	8.3	4.0
	With proposed	25.4	931	24	400	32.3	31.0

Note: "*" marks the matching method in [2] and [14].
"**" the current data in the table are peak-to-peak values.

and compared with previous methods in Table V. Both of these two hardware experimental platforms are built based on a DSP TMS320F28335 controller is constructed. The sensors collect current and voltage signals and transfer them to DSP for proposed compromised ideal reference calculations. Based on the comparison between the calculated ideal reference current and the measured current, the trigger signals of IGBT G_1–G_4 in the full H-bridge can be generated to finish the whole control process and experiments.

Fig. 10 shows the transmitter output voltage v_s, load current i_L, and dc voltage V_{dcc} without impedance matching in a) and b), with previous impedance matching in [2] and [14] in c) and d), and with proposed compromised control in e) and f). Higher load current i_L presents better matching results and higher SNR in geological prospecting. But higher dc voltage V_{dcc} means more difficult to realize. In Fig. 10(a) and (b), only fundamental compensating is realized, and the high-frequency reactive power is still unmatched. The results of the previous method [2] and [14] to compensate for all frequencies are shown in Fig. 10(c) and (d). Fig. 10(c) and (d) compensates for reactive power at all frequencies, and i_L under 100 Hz, 200 Hz, and 300 Hz has been increased by 29.8%, 19.6%, and 8.3%, respectively. However, the required dc supply voltage is improved from 300 V to 700 V since the amount of reactive power compensation for each frequency is not optimally calculated. The large and unreasonable amount of reactive power compensation requires high dc voltage. Comparatively, the results of compensating with

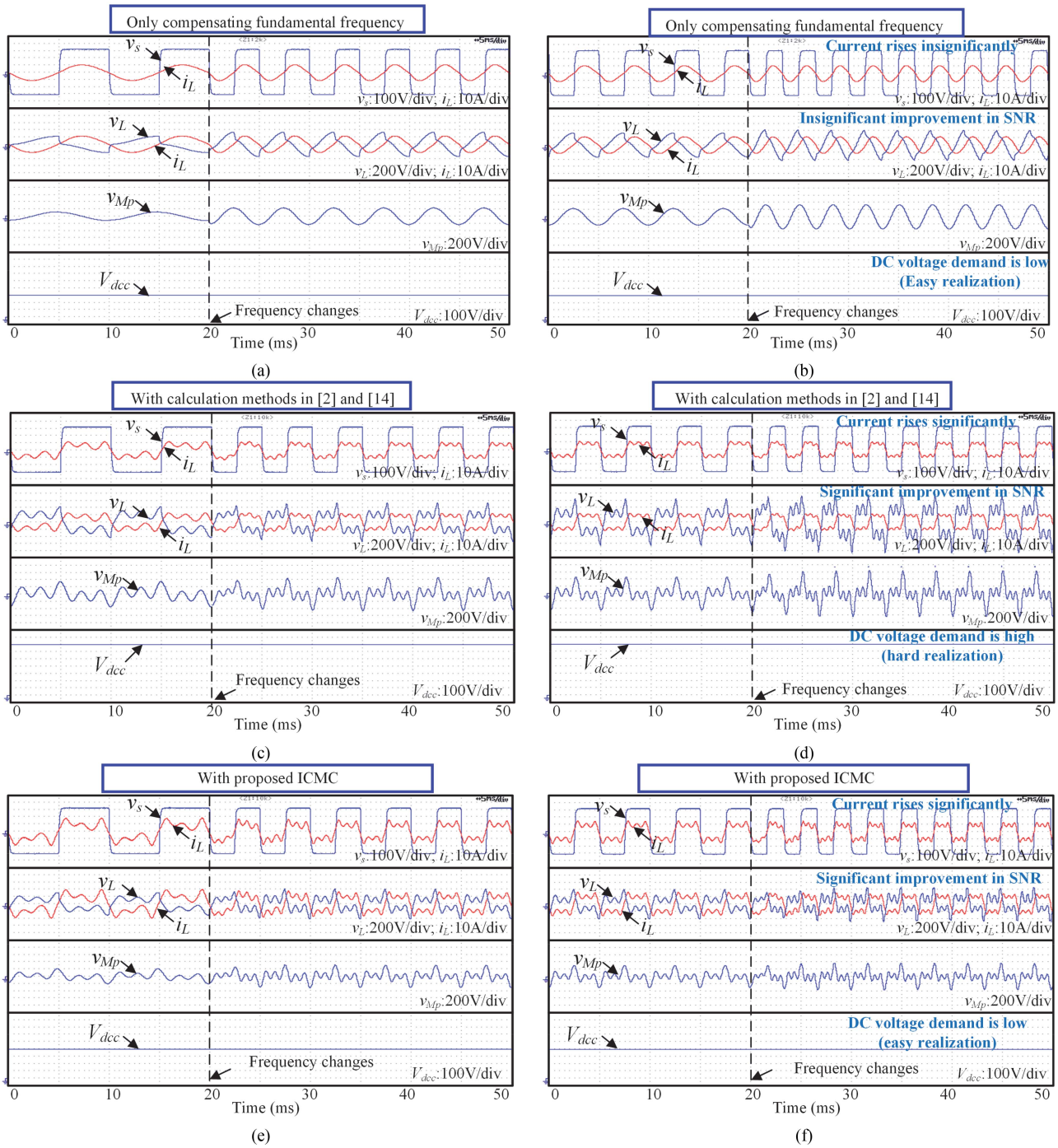

Fig. 10. Comparative dynamic experimental compensating waveforms: (a) without impedance matching from 100 Hz v_s to 200 Hz v_s; (b) without impedance matching from 200 Hz v_s to 300 Hz v_s; (c) with previous linear impedance matching method [2] and [14] from 100 Hz v_s to 200 Hz v_s; (d) with previous linear impedance matching method [2] and [14] from 200 Hz v_s to 300 Hz v_s; (e) with proposed ICMC and compromised control method from 100 Hz v_s to 200 Hz v_s; (f) with proposed ICMC and compromised control method from 200 Hz v_s to 300 Hz v_s.

the proposed linear reference calculation method in Fig. 10(e) and (f) can realize i_L increase under 100 Hz, 200 Hz, and 300 Hz has been increased by 29.8%, 19.6%, and 8.3%, respectively. Dc supply voltage reduced to 400 V. Because the amount of reactive power compensation is optimized to realize the highest i_L increase with per-unit $V_{\mathrm{dc}\,c}$, the SNR satisfies the requirement with minimum dc. In addition, the voltage waveforms for G_1 to G_4 when the proposed ICMC compensates the load in 200 Hz v_s as Fig. 11.

Overall, the i_L increasing with per-unit V_{dc} has been improved by 31.0%–65.5% with the proposed calculation method. The results verify the feasibility and advantages of the proposed compromised control and its injection circuit coupling realization methods.

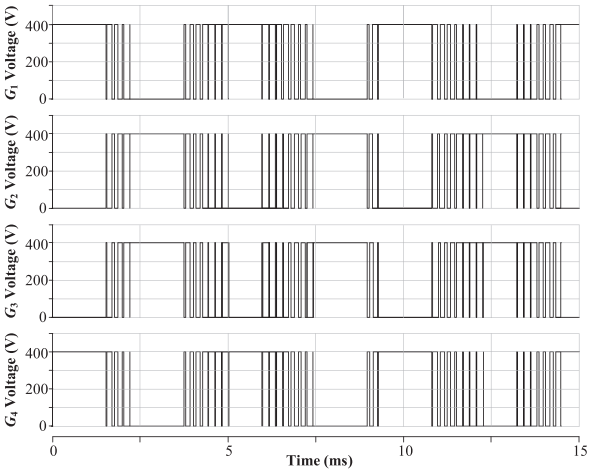

Fig. 11. Voltage waveforms for G_1 to G_4 when the proposed ICMC compensates the load in 200 Hz v_s.

VI. Conclusion

This article focuses on reactive power compensation and impedance matching of nonlinear square-wave voltages. The difficulty in the theoretically ideal matched current calculation is solved by proposing a compromised optimization method. The impedance matching reference is considered in compromised with the hardware limitation to balance the performance and hardware requirement. The proposed ideal matched current calculation method determines the control objective, achieving the minimum dc voltage requirement based on SNR requirements for detection. With the optimized amount of reactive power compensation at each frequency order, 31.0%–65.5% more i_L improvement with per-unit $V_{\mathrm{dc}\,c}$ increasing is realized compared to previous methods to compensate reactive power at all frequencies.

Appendix

A. Power Loss Analysis

The principle of ICMC to improve the energy utilization of the transmitter is injecting variables of reactive power to offset the reactive power of the load. When ICMC only injects reactive power, from the perspective of energy, theoretically, there is no active power reactive power consuming, and the reactive power does not do work. Reactive power is the power component used to establish electric and magnetic fields and conduct energy exchange between electrical equipment. It is not like active power that is consumed and converted into other forms of energy (such as mechanical energy and thermal energy) to complete actual work.

However, the ICMC itself will have a small amount of power losses during operation. These losses mainly include the conduction losses and switching losses of switching devices, as well as line losses. The main energy losses come from the following two aspects: 1) power switching devices such as IGBTs in the ICMC will consume a certain amount of energy during the turn-ON and turn-OFF processes, which is called switching power loss; 2) When current passes through the inductor and capacitor and other components of the ICMC, due to the resistance of these components themselves, a certain amount of power loss (I^2R loss) will also be generated; 3) When the alternating magnetic field through the iron core, it will produce an induced electromotive force inside the core. Extra energy is needed to overcome the hysteresis phenomenon. This part of the energy is lost in the form of heat, known as hysteresis loss. In addition, the continuous eddy currents in the iron core also will produce thermal loss. By referring to most current studies on reactive power compensators, the efficiency of reactive power compensators is usually above 95%. That is, for every 1 kVar of reactive power injected, there is 50 W of power loss.

TABLE VI
Calculated Power Loss When Injecting 700 Var Reactive Power

Type of power loss	DC-link voltage V_{dcc} (V)	Power loss (W)
Switching power loss	700	21.1
	400	12.1
Conduction power loss	700/ 400	2.5
Transformer iron loss	700/ 400	4.2
Total power loss	700	27.8
	400	18.8

a) Switching Power Loss: Switching power losses are the main thermal losses of power converter [24]. The switching losses of a converter depend mainly on the voltage loaded across the switches and the current passing through them. Generally speaking, the switching losses of a converter can be modeled as [25]

$$P_{\mathrm{loss}(sw)} = V_{\mathrm{dc}} I_{\mathrm{loss}} = V_{\mathrm{dc}} I_{CM} f_{sw} \left(\frac{1}{8} t_{rN} \frac{I_{CM}}{I_{CN}} + t_{fN} \left(\frac{1}{3\pi} + \frac{1}{24} \frac{I_{CM}}{I_{CN}} \right) \right) \tag{32}$$

where I_{CM}, I_{CN}, t_{rN}, and t_{fN} are the maximum collector current, the rated collector current, the rated rise time, the rated fall time, and the switching frequency, respectively. Based on the settings of the user's manual of the IGBT selected in this article, parameters on the components [27], the parameters of (32) are given as follows $V_{\mathrm{dc}\,c} = 400$ V, $I_{CM}/I_{CN} = 0.9$, $f_{sw} = 10$ kHz, $t_{rN} = 0.18$ μs, $t_{fN} = 2.2$ μs. When the ICMC is controlled to generate 700 Var reactive power, $\mathrm{I_{CM}}$ is equal to 7 A. Based on the above data, the efficiency of ICMC can be calculated. The calculation results are listed in Table VI. The switching power losses account for 1.7%– 3.0% of the total output reactive power.

b) Component Conduction Loss: Component conduction power loss is another source of power loss, except for switching power loss. Because when the current passes through the components, the parasitic resistance in the components causes heat generation and leads to losses. Component conduction loss of L_c, C_p, and M_p can be calculated by [22]

$$\begin{aligned} P_{\mathrm{loss(comp)}} &= P_{\mathrm{loss}(L_c)} + P_{\mathrm{loss}(C_p)} + P_{\mathrm{loss}(L_p)} + P_{\mathrm{loss}(M_p)} \\ &= \left(\mathrm{ESR}_{L_c} + \mathrm{ESR}_{C_p} + \mathrm{ESR}_{L_p} + \mathrm{ESR}_{M_p} \right) \cdot I_L^2 \end{aligned} \tag{33}$$

where ESR is the equivalent series resistance (ESR) of energy storage elements such as capacitors and inductors. Ideal capacitors and inductors only have capacitive or inductive characteristics with no energy loss. However, actual capacitors and inductors will have some resistive components due to materials, manufacturing processes, and other factors. According to the IEEE standards, IEEE Std. 38-2020 and Std. 284-2021 about the ESR of converter coupling components [26], the total ESR coupling components should be less than 1 Ω. Since the value of ESR is affected by a variety of factors of the inductor and capacitor components, there is no accurate formula to calculate. Specific ESR values can be obtained by looking up the user manuals of the hardware used. The ESR of the devices used in this article are as follows: $\mathrm{ESR}_{Lc} = 0.015\ \Omega$, $\mathrm{ESR}_{Cp} = 0.02\ \Omega$, $\mathrm{ESR}_{Lp} = 0.015\ \Omega$, and $\mathrm{ESR}_{Mp} = 1\ \Omega$ [28]. Based on the above data, the conduction loss caused by the ESR of different components can be calculated. Table VI lists the calculated results of component conduction loss, which accounts for 0.35% of the total output reactive power.

c) Transformer Iron Loss: In particular, for transformers, there is a part of the iron loss in addition to the conduction loss. And the iron loss is composed of hysteresis loss and the eddy-current loss. Hysteresis loss $P_{\mathrm{loss}Mp(h)}$ is the energy loss that occurs due to the repeated orientation of magnetic domains in ferromagnetic materials under the influence of an alternating magnetic field, which can be calculated by (34) [30]. In addition, when an alternating magnetic flux passes through the core, an induced electromotive force is generated inside the core, which in turn forms a swirling current known as an eddy current. The loss that occurs due to these eddy currents on the resistance of the core is the eddy-current loss. The eddy-current loss $P_{\mathrm{loss}Mp(e)}$ is usually calculated through (35) [31]

$$P_{\mathrm{loss}Mp(h)} = K_h f B_m^n V \tag{34}$$

$$P_{\mathrm{loss}Mp(e)} = K_e f^2 B_m^2 t^2 V \tag{35}$$

where the parameters can be obtained by consulting the user manual [29] of the transformer: the hysteresis loss coefficient $K_h = 20\ \mathrm{J/m^3}$, the maximum magnetic flux density $B_m = 1$ T, the core volume $V = 0.01\ \mathrm{m^3}$, the transformer ratio is 1, eddy current loss coefficient $K_e = 10\ \mathrm{J/m^3}$, and the thickness of the silicon steel sheet $t = 0.5$ mm. Based on the above data, the transformer iron loss, including the hysteresis loss and the eddy-current loss, can be calculated. Table VI gives the calculated results of transformer iron loss, which accounts for 0.60% of the total output reactive power.

In summary, ICMC does not inject active power to improve the output power of the transmitter. In ideal conditions, through the reactive power injected by ICMC, the transmitter can only output active power. Provided that the transmitter capacity is certain, the output power and energy utilization are maximized at this ideal condition. Because theoretically, reactive power is produced without consuming active power. In fact, the efficiency of the power converter in generating reactive power is more than 95%. Only a small amount of active power is consumed to produce the compensating reactive power. Thus, the improvement of the energy of the transmitter is much larger than the consumed active power by ICMC.

TABLE VII
COMPUTATIONAL PROCESSES IN THE CONTROL METHOD

Calculation step	Details of calculation
Step 1*	Calculate the FFT of v_s, i_{noi}, and i_L
Step 2*	Calculate reference SNR^*_{iLn} based on the sampling i_{noi} and i_L
Step 3**	Calculate the reference voltage v^*_L, v^*_{Cp}, v^*_{Lp}, v^*_{Mp}, v^*_{Mp1}, and v^*_{inv}
Step 4**	Calculate the G_1– G_4 PWM signals by comparing v^*_{inv} and carrier wave

Note: "*" marks the steps of precomputation algorithm.
"**" marks the steps of real-time control processes with PWM.

TABLE VIII
NUMBER OF CALCULATION OPERATIONS IN THE CONTROL METHOD

Control step		Number of calculation operation					
		+	-	×	/	√x	>
Precomputation	Step 1*	34	9	324	9	9	--
	Step 2	2	6	4	2	2	--
	Operation number	36	15	328	11	11	--
Real-time computation	Step 3	20	3	21	--	--	--
	Step 4	--	4	--	--	--	4
	Operation number	20	7	21	--	--	4

**Note:* FFT operation is calculated up to 9th harmonics.

B. Calculation Time Analysis of Proposed Control Method

The full calculation steps of the proposed control method are summarized in Table VII. Based on the computational processes listed in Table VIII, the required number of mathematical operations of the proposed control method can be counted. It should be noted that not all steps of computations are executed in real time with PWM. Steps 1 and 2 are the steps of the precomputation algorithm, which can be finished before real-time control. Because the noise and detection load characteristics in the environment do not change significantly over a period of time. Steps 3 and 4 are the real-time control processes executed with PWM.

Then, the time required to complete a control loop can be derived from the total number of mathematical operations required and the time required to complete a single mathematical operation by DSP. The required number of basic calculation operations in the precomputation algorithm of the proposed control method is counted in Table VIII. It is important to note that there are many ways to implement FFT using DSP, and a common algorithmic implementation is used here. To perform an FFT operation with an order number n, $4n^2$ multiplications and $(4n\text{-}2)$ additions are required [33].

As shown in Table VIII, based on the number statistics of calculation operations in the proposed control method, the main calculation operations are focused on the FFT process in step 1. The calculation operations for the remaining processes are relatively minimal. The DSP processor model used in this paper is TMS320F28379D. According to the user manual of DSP [33], the operating frequency of the TMS320F28379D chip is 200 MHz. This means that there are $200\times\ 10^6$ clock cycles per second. For addition, subtraction, and comparison operations, ideally, a single-cycle instruction can complete one operation within one clock cycle. Calculated at a maximum clock frequency of 200 MHz. Theoretically, 200×10^6 addition or subtraction operations can be performed per second.

TABLE IX
CALCULATION TIME OF THE CONTROL METHOD

Control step		Time of calculation operation (μs)					
		+	-	×	/	√x	>
Precomputation	Step 1	0.17	0.045	4.85	0.45	5.01	--
	Step 2	0.01	0.03	0.060	0.1	1.10	--
	Total time	0.18	0.075	4.91	0.55	6.11	--
Real-time computation	Step 3	0.1	0.015	0.32	--	--	--
	Step 4	--	0.02	--	--	--	0.02
	Total time	0.1	0.035	0.32	--	--	0.02

Multiplication and division operations typically require multiple clock cycles. For example, in some DSP implementations, a multiplication may take 3 clock cycles, and a division may take 10 cycles. So, approximately 66.7×10^6 multiplication and 20×10^6 division operations can be performed per second. The root operation is usually implemented through the Newton–Raphson iteration method. Generally, one Newton Raphson iteration may require 2 multiplications, 2 additions, and 1 division. A root operation requires 4 iterations to calculate, so approximately 1.79×10^6 times square root operation can be performed per second [34]. Based on the above analysis of DSP calculation speed and the number of DSP calculation operations in each step, the calculation time for each step and total calculation time can be concluded in Table IX.

Generally, for the control part of the converter, it is required that the calculation time be less than the PWM cycle. If the PWM frequency is set as 10 kHz and the cycle is set as 100 μs. Thus, no matter the calculation time of the precomputation part or the real-time computation part is much smaller than the PWM cycle.

C. Signal Frequency, Power, and Magnetic Field Range of Electromagnetic Prospecting System

a) Signal Frequency: The detection frequency is mainly determined by the depth of the detection target, and different geological targets have different responses to electromagnetic signals of different frequencies. Usually, high-frequency signals are used for shallow detection targets [7]. This is because the skin effect of high-frequency electromagnetic waves is obvious, and the energy is concentrated near the ground surface. The skin effect can be expressed by the skin depth

$$\delta = \sqrt{\frac{1}{\pi f \mu \sigma}} \tag{36}$$

where δ is the detection depth, f is the signal frequency, μ is the magnetic permeability, and σ is the electrical conductivity. Equation (36) indicates that the higher the frequency, the smaller the skinning depth, and the signal is concentrated in shallow propagation; the lower the frequency, the greater the skinning depth, and the signal can penetrate deeper strata. In order to more intuitively represent the relationship between frequency and detection depth, the relationship between commonly used detection frequencies and corresponding depths is summarized in the following Table X. Therefore, the 100–300 Hz transmitting voltage frequency chosen for the experiments in this paper corresponds to a detection depth of approximately 350–200 m.

TABLE X
RELATIONSHIP BETWEEN FREQUENCY AND DETECTION DEPTH

Detection depth δ (m)	Signal frequency f (Hz)
200	316
250	202
300	140
350	103

b) Power: The degree of signal attenuation is related to the distance [2]. The signal attenuation formula is usually calculated through

$$P_r = P_t \cdot e^{-\alpha \cdot d} \tag{37}$$

where P_r is the received power, P_t is the transmitted power, α is the attenuation coefficient depending on the geological condition, and d is the propagation distance. In electromagnetic detection, as the depth of detection (propagation distance) increases, the received power decreases exponentially. It is necessary to determine the appropriate transmit power based on the attenuation coefficient in order to ensure sufficient received power for detection. At the same time, the SNR of the received power is also necessary to take into account, usually, it is desired to achieve an SNR larger than 5 dB

$$\mathrm{SNR}_{P_r} = 10 \lg \frac{P_r}{P_{noi}} \tag{38}$$

where P_{noi} is the power of noise. Thus, deep detection requires higher transmitter power. Combining (37) and (38), the needed transmitted power P_t can be approximately calculated.

c) Magnetic Field Range: The magnetic field range can be calculated using the Biot–Saval law [5]. The formula is given as

$$\vec{B} = \frac{\mu_0}{4\pi} \int \frac{I_L d\vec{l} \times \vec{r}}{r^3} \tag{39}$$

where $\vec{B}$ is the magnetic field strength, μ_0 is the vacuum permeability, I_L is the current, $d\vec{l}$ is the current element length vector, and $\vec{r}$ is the position vector from the current element to the point of observation. Based on (39), the Magnetic Field Range $\vec{r}$ can be calculated based on magnetic field strength and other above values.

d) Explanations of Using Square Voltage: First of all, sinusoidal voltage can be used for electromagnetic detection. According to the laws of electromagnetic induction and Maxwell's equations, when the antenna is added with a sinusoidal voltage, the electromagnetic field can also be generated. Essentially, sinusoidal voltage is a kind of ac voltage.

However, square-wave voltages are currently the most commonly used in practical detection [8]. This is mainly because square waves and sinusoidal waves have different spectra. A square wave contains multiple harmonic components, while a sinusoidal wave contains only a unique dominant frequency component, as shown in Fig. 3. Based on the above discussion of signal frequency and (36), signals of different frequencies correspond to different detection depths. Using a square-wave voltage with multiple harmonic components can detect the subsurface at multiple depths in a single survey. Because the detection usually

requires the characterization of the subsurface over a range of depths. Therefore, the usage of square-wave voltages can greatly improve the efficiency of detection.

REFERENCES

[1] X. Zhang, X. Pang, S. Yu, and Y. Pang, "A broadband multifrequency resonance compensator for frequency-domain electromagnetic prospecting transmitting system," *IEEE Trans. Power Electron.*, vol. 39, no. 5, pp. 5178–5193, May 2024.

[2] Y. Pang et al., "A multiple frequency spectrum impedance matching method of nonlinear geological surveying electromagnetic method for power amplifier capacity utilization enhancement," *IEEE Trans. Ind. Electron.*, vol. 72, no. 1, pp. 366–379, Jan. 2025, doi: 10.1109/TIE.2024.3409868.

[3] B. Su, J. Yu, G. M. Królczyk, P. Gardoni, and Z. Li, "Innovative surface-borehole transient electromagnetic method for sensing the coal seam roof grouting effect," *IEEE Trans. Geosci. Remote Sens.*, vol. 60, 2022, Art. no. 5702509.

[4] M. Wang, S. Jin, M. Deng, W. Wei, and K. Chen, "Multifunction electromagnetic transmitting system for mineral exploration," *IEEE Trans. Power Electron.*, vol. 33, no. 10, pp. 8288–8297, Oct. 2018.

[5] J. Chen, Y. Zhang, and T. Lin, "Transient electromagnetic machine learning inversion based on pseudo wave field data," *IEEE Trans. Geosci. Remote Sens.*, vol. 60, 2022, Art. no. 5917410.

[6] X. Zhang, X. Pang, W. Liu, S. Yu, and G. Li, "A novel optimization method for SHEPWM-based depth-focused electromagnetic transmitting system," *IEEE Trans. Instrum. Meas.*, vol. 72, 2023, Art. no. 2006813.

[7] L. Liu, J. Li, L. Huang, X. Liu, and G. Fang, "Double clamping current inverter with adjustable turn-off time for bucking coil helicopter transient electromagnetic surveying," *IEEE Trans. Ind. Electron.*, vol. 68, no. 6, pp. 5405–5414, Jun. 2021.

[8] T. Li, M. Zhang, and J. Lin, "Three-dimensional forward modeling of ground wire source transient electromagnetic data using the meshless generalized finite difference method," *IEEE Trans. Geosci. Remote Sens.*, vol. 61, 2023, Art. no. 2002913.

[9] A. Al Bastami, A. Jurkov, D. Otten, D. T. Nguyen, A. Radomski, and D. J. Perreault, "A 1.5 kW radio-frequency tunable matching network based on phase-switched impedance modulation," *IEEE Open J. Power Electron.*, vol. 1, pp. 124–138, 2020.

[10] J. He, Y. W. Li, and F. Blaabjerg, "An enhanced islanding microgrid reactive power, imbalance power, and harmonic power sharing scheme," *IEEE Trans. Power Electron.*, vol. 30, no. 6, pp. 3389–3401, Jun. 2015.

[11] M. Esmaili, M. Ghamsari-Yazdel, N. Amjady, C. Y. Chung, and A. J. Conejo, "Transmission expansion planning including TCSCs and SFCLs: A MINLP approach," *IEEE Trans. Power Syst.*, vol. 35, no. 6, pp. 4396–4407, Nov. 2020.

[12] S. Naderi, M. Javadi, M. Mazhari, and C. Y. Chung, "A machine learning-based framework for fast prediction of wide-area remedial control actions in interconnected power systems," *IEEE Trans. Power Syst.*, vol. 38, no. 1, pp. 242–255, Jan. 2023.

[13] J. Yu, L. Wang, W. Tian, K. Zhang, S. Liao, and Q. Xu, "An adaptive broadband active impedance matching network for underwater electroacoustic transduction system," *IEEE Trans. Ind. Electron.*, vol. 70, no. 6, pp. 5433–5443, Jun. 2023.

[14] W. Tian et al., "A hybrid impedance matching network for underwater acoustic transducers," *IEEE Trans. Power Electron.*, vol. 38, no. 6, pp. 7622–7633, Jun. 2023.

[15] H. Zhou, S. H. Huang, and W. Li, "Electrical impedance matching between piezoelectric transducer and power amplifier," *IEEE Sensors J.*, vol. 20, no. 23, pp. 14273–14281, Dec. 2020.

[16] M. Wang, S. Jin, M. Deng, W. Wei, and K. Chen, "Multifunction electromagnetic transmitting system for mineral exploration," *IEEE Trans. Power Electron.*, vol. 33, no. 10, pp. 8288–8297, Oct. 2018.

[17] Z. Huang, T. Qin, X. L. Li, L. Ding, H. H.-C. Iu, and C. K. Tse, "Synthesis of inductive power transfer converters with dual immittance networks for inherent CC-to-CV charging profiles," *IEEE Trans. Power Electron.*, vol. 39, no. 6, pp. 7766–7777, Jun. 2024.

[18] X. L. Li, Y. C. Liu, C. K. Tse, and C. Zhu, "Integrated multiple compensation circuits for wireless power transfer with fewer components," *IEEE Trans. Ind. Electron.*, vol. 71, no. 8, pp. 8892–8902, Aug. 2024.

[19] X. Zhang, S. Yu, G. Li, and Y. Pang, "A nonlinear hybrid impedance matching technique for electromagnetic exploration transmitter with 96% multi-frequency signal energy utilization," *IEEE Trans. Power Electron.*, vol. 39, no. 12, pp. 15880–15897, Dec. 2024, doi: 10.1109/TPEL.2024.3446820.

[20] N. Limsupavanich, B. Guo, and X. Fu, "Improvement of coastal sea-level altimetry derived from GNSS SNR measurements using the SNR forward network and T-LSTM anomaly detection," *IEEE Trans. Geosci. Remote Sens.*, vol. 60, 2022, Art. no. 5803513.

[21] J. Yu, H. Shen, H. Wang, and X. Wu, "Speed estimation of multiphase induction motor using rotor slot harmonics with limited SNR and dynamic load conditions," *IEEE Trans. Ind. Electron.*, vol. 70, no. 7, pp. 6618–6631, Jul. 2023.

[22] M.-C. Wong, Y. Pang, Z. Xiang, L. Wang, and C.-S. Lam, "Assessment of active and hybrid power filters under space vector modulation," *IEEE Trans. Power Electron.*, vol. 36, no. 3, pp. 2947–2963, Mar. 2021.

[23] Y. Pang, M.-C. Wong, G. Li, H. Zhou, and J. Lin, "Fusion multilevel hybrid multi-VSC topology's m-to-1 rating design for current sharing with reduced capacity and enhanced efficiency," *IEEE Trans. Ind. Electron.*, vol. 71, no. 8, pp. 8291–8303, Aug. 2024.

[24] Y. Pang et al., "A fusion topology of higher efficiency and lower capacity hybrid parallel multi-converters for power quality compensation," *IEEE Trans. Power Electron.*, vol. 37, no. 5, pp. 5957–5969, May 2022.

[25] L. Wang, C.-S. Lam, and M.-C. Wong, "Minimizing inverter capacity design and comparative performance evaluation of SVC-coupling hybrid active power filters," *IEEE Trans. Power Electron.*, vol. 34, no. 2, pp. 1227–1242, Feb. 2019.

[26] *IEEE Recommended Practice for Testing Transformers and Inductors for Electronics Applications*, IEEE Standard 389-2020, (Revision IEEE Standard 389–1996), IEEE, May 2020, doi: 10.1109/IEEESTD.2020.9084213.

[27] "Infineon technologies FD500R65KE3KNOSA1," Digikey Electronics, 2023. [Online]. Available: https://www.digikey.com/en/products/detail/FD500R65KE3KNOSA1/

[28] Hammond Manufacturing 195E100, "Digikey electronics," 2023. [Online]. Available: https://www.digikey.com/en/products/detail/hammondmanufacturing/195E100/455623

[29] Power transformers 68-25, "Digikey electronics," 2023. [Online]. Available: https://www.digikey.com/en/products/detail/signal-transformer/68-25/1984779

[30] A. Rezaei-Zare, "Reactive power loss versus GIC characteristic of single-phase transformers," *IEEE Trans. Power Del.*, vol. 30, no. 3, pp. 1639–1640, Jun. 2015.

[31] X. Zhang, X. Liu, F. Guo, G. Xiao, and P. Wang, "Calculation of DC bias reactive power loss of converter transformer via finite element analysis," *IEEE Trans. Power Del.*, vol. 36, no. 2, pp. 751–759, Apr. 2021.

[32] Y. Chen, M. Chen, L. Xu, and Z. Liang, "Chance-constrained optimization of storage and PFC capacity for railway electrical smart grids considering uncertain traction load," *IEEE Trans. Smart Grid*, vol. 15, no. 1, pp. 286–298, Jan. 2024.

[33] Y. Wang, Y. Tang, Y. Jiang, J.-G. Chung, S.-S. Song, and M.-S. Lim, "Novel memory reference reduction methods for FFT implementations on DSP processors," *IEEE Trans. Signal Process.*, vol. 55, no. 5, pp. 2338–2349, May 2007.

[34] TMS320F28379, "Texas instruments," 2024. [Online]. Available: https://www.ti.com.cn/product/cn/TMS320F28379D

[35] C. A. Sepúlveda, J. A. Muñoz, J. R. Espinoza, M. E. Figueroa, and C. R. Baier, "FPGA v/s DSP performance comparison for a VSC-based STATCOM control application," *IEEE Trans. Ind. Inform.*, vol. 9, no. 3, pp. 1351–1360, Aug. 2013.

Ying Pang (Member, IEEE) received the B.Sc. degree in electrical engineering from Southwest Jiaotong University, Chengdu, China, in 2015, and the M.Sc. and Ph.D. degrees in electrical and computer engineering from the University of Macau, Macao, China, in 2018 and 2022, respectively.

In 2022, he was with Jilin University, Changchun, China, where he is currently a Postdoctoral Fellow. His research interests include power electronics equipment in geological exploration, power filter, smart grid, renewable energy, power converter, and distributed generation.

Dr. Pang was the recipient of the first prize of the Guangdong Electric Power Science and Technology Paper Award in 2022 and the recipient of the silver medal of the second China Postdoctoral Innovation and Entrepreneurship Competition in 2023.

Yanju Ji received the M.S. degree in measurement technology and instrument and the Ph.D. degree in earth exploration and information techniques from Jilin University, Changchun, China, in 1998 and 2004, respectively.

From 2004 to 2009, she was an Associate Professor with Jilin University. Since 2010, she has been with Jilin University where she is currently a Professor of instrument science and technology. She has authored or coauthored more than 200 articles. Her current research interests include computational electromagnetics, inverse problems, and electromagnetic detecting instrument.

Xinhao Zhang received the B.S. and M.S. degrees in electrical engineering from Jilin University, Changchun, China, in 2019 and 2022, respectively, where he is currently working toward the Ph.D. degree in electrical engineering.

His research interests include the design and implementation of high-power transmission sources.

Yongji Zhu received the B.Sc. degree in electrical engineering from Jilin University, Changchun, China, in 2023. He is currently working toward the Ph.D. degree in control science and engineering with Jilin University, Changchun, China.

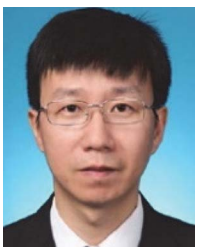

Gang Li (Member, IEEE) received the Ph.D. degree in electrical engineering from Tsinghua University, Beijing, China, in 2009.

He is currently a Full Professor with the College of Instrumentation and Electrical Engineering, Jilin University, Changchun, China. His research interests include modeling of semiconductors and Li batteries, matrix converters, dc–dc power converter and its applications in electromagnetic detection instruments, and design and implementation of high power source.

Cheng Gong (Member, IEEE) received the M.Sc. degree in electrical engineering from Guangxi University, Nanning, China, in 2017, and the Ph.D. degree in electrical and computer engineering from the University of Macau (UM), Macau, China, in 2022.

He was currently a Postdoctoral Fellow with the Institute of Microelectronics, UM, until 2023. He is currently a Research Assistant Professor with the Institute of Microelectronics, UM. His research interests include power quality, converter controller design, and power electronic based power systems.

Zeng Xiang (Member, IEEE) received the B.Sc. degree in electrical engineering and automation from the Tianjin University of Science and Technology, Tianjin, China, in 2009, the M.Sc. degree in electronic engineering from Hunan University, Changsha, China, in 2012, and the Ph.D. degree in electrical from the University of Macau, Macau, China, in 2023.

From 2012 to 2015, he was an R&D Engineer with Zhuhai Wanlida Electrical Automation Company Ltd., Zhuhai, China.

Since 2023, he has been with the Aerospace Yinshan Electric Company Ltd, Zhuhai, China, as the Chief Technology Officer. His research interests include high-performance converters for microgrids, power quality, and distributed power generation system.

Rong Han (Member, IEEE) was born in Gansu, China, in 1995. She received the B.S. degree in electrical engineering and automation and the Ph.D. degree in electrical engineering from Hunan University, Changsha, China, in 2017 and 2022, respectively.

From 2022 to 2024, she was a power electronics R&D engineer with Tebian Electric Apparatus Stock Company Ltd. She is currently an Assistant Professor with School of Optoelectronic Engineering and instrumentation science, Dalian University of Technology, Dalian, China. Her research interests include high-power special power supply and converter control technology, active thermal control, multilevel converters, model predictive control, and application technology of GaN-based power devices.

Haigen Zhou (Member, IEEE) was born in Henan, China, in 1990. He received the B.S. degree in electrical engineering and automation and the Ph.D. degree in measurement technology and instruments from Jilin University, Changchun, China, in 2012 and 2017, respectively.

He is currently a Lecturer with Jilin University. His research interests include ground-airborne frequency-domain electromagnetic instruments and their applications.

Man-Chung Wong (Senior Member, IEEE) received the B.Sc. and M.Sc. degrees in electrical and electronics engineering from the University of Macau (UM), Macao, China, in 1993 and 1997, respectively, and the Ph.D. degree in electrical engineering from Tsinghua University, Beijing, China, in 2003.

He is currently a Professor and the Department Head with the Department of Electrical and Computer Engineering, University of Macau. He was a visiting fellow with Cambridge University. He is currently affiliated with the State Key Laboratory of Internet of Things for Smart City and the State Key Laboratory of Analog and Mixed Signal VLSI, University of Macau, Macao, China. He has authored and coauthored four books and more than 180 technical journals (more than 70 SCI papers) and conference papers and holds four U.S. patents and eight Chinese patents. His research interests include integrated power electronics controllers, power electronics converters, power quality compensators, renewable energy, wireless power transfer, and smart grid.

Dr. Wong was a recipient of Second Class 2022 Macao Science and Technology Natural Science Award, the Macao Science and Technology Invention Awards (2nd Class in 2018, 3rd Class in 2014 and 2012, respectively), and the Young Scientist Award from "Instituto International De Macau" at 2000, Young Scholar Award from the University of Macau in 2001, Second Prize of 2003 Tsinghua University Excellent Doctor Thesis Award. He was IEEE TENCON Macao 2015 General Chair and IEEE APPEEC Macao 2019 General Chair. He was Chair of the IEEE Macau Section in 2014 and 2015, and he was a chair of the IEEE Macau PES/PELS Joint Chapter between 2015 and 2020. He has been an IEEE Region 10 Power and Energy Society North Representative since 2015. He is the Institution of Engineering and Technology fellow since 2023.

Jun Lin received the B.S. and M.S. degrees in applied geophysics from the Changchun College of Geology, Changchun, China, in 1982 and 1987, respectively.

He is currently a Professor with the College of Instrumentation and Electrical Engineering, Jilin University, Changchun, China. He is the Director with the National Geophysical Exploration Equipment Engineering Research Center, Jilin University, Changchun, China. He is also an Academician with the Chinese Academy of Engineering, Beijing, China. His research interests include geophysical exploration theory, technologies, and equipment.